Flexible Single-Crystal Silicon Nanomembrane Photonic Crystal Cavity

Xiaochuan Xu,[*,†,‡,#] Harish Subbaraman,[‡,#] Swapnajit Chakravarty,[‡] Amir Hosseini,[‡] John Covey,[†] Yalin Yu,[§] David Kwong,[†] Yang Zhang,[†] Wei-Cheng Lai,[†] Yi Zou,[†] Nanshu Lu,[§] and Ray T. Chen[*,†]

[†]Microelectronics Research Center, The University of Texas at Austin, 10100 Burnet Road, Bldg. 160, Austin, Texas 78758, United States, [‡]Omega Optics, Inc. 8500 Shoal Creek Drive, Bldg. 4, Suite 200, Austin, Texas 78757, United States, and [§]Department of Aerospace Engineering and Engineering Mechanics, Center for Mechanics of Solids, Structures and Materials, Texas Materials Institute, The University of Texas at Austin, Austin, Texas 78712, United States. [#]Authors X.X. and H.S. contributed equally to this work.

ABSTRACT Flexible inorganic electronic devices promise numerous applications, especially in fields that could not be covered satisfactorily by conventional rigid devices. Benefits on a similar scale are also foreseeable for silicon photonic components. However, the difficulty in transferring intricate silicon photonic devices has deterred widespread development. In this paper, we demonstrate a flexible single-crystal silicon nanomembrane photonic crystal microcavity through a bonding and substrate removal approach. The transferred cavity shows a quality factor of 2.2×10^4 and could be bent to a curvature of 5 mm radius without deteriorating the performance compared to its counterparts on rigid substrates. A thorough characterization of the device reveals that the resonant wavelength is a linear function of the bending-induced strain. The device also shows a curvature-independent sensitivity to the ambient index variation.

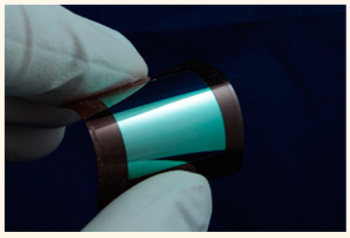

KEYWORDS: silicon nanomembrane · photonic crystal · photonic crystal cavity · flexible inorganic devices · wafer bonding

Developing flexible single-crystal silicon electronics and photonics is a modern instance of the archetypal human *versus* nature conflict. The enthusiasm of this effort is stimulated by a natural quandary: the well-established integrated electronics and photonics are manufactured on silicon-based substrates, which are rigid; on the contrary, all organisms are soft and curvilinear. This seemingly intrinsic incompatibility is resolved by the discovery that nanomembranes with thickness less than a few hundred nanometers can have flexural rigidities more than 15 orders of magnitude smaller than those of bulk wafers (>200 μm) of the same materials.[1,2] A hybrid platform which enjoys both the high performance of inorganic materials and the flexibility of organic materials is believed to have a vast range of unprecedented applications which could not be implemented by either inorganic or organic platforms alone. Since direct growth of single-crystal silicon on curvaceous and conformable organic surfaces is not possible, a hybrid platform is usually formed by physically transferring single-crystal silicon nanomembranes onto flexible plastic substrates.[3−16] Although still in its infancy, this hybrid approach has been extensively explored for applications in epidermal electronics,[3,13] implantable devices,[4,8,9] flexible silicon integrated circuits,[5,12,16] flexible solar cells,[10] bionic devices,[14] *etc.*

This hybrid platform also paves the way for flexible silicon photonics. Single-crystal silicon also has superior optical properties at telecommunication wavelengths, including a high refractive index and extremely low absorption loss, the likes of which cannot be obtained with organic materials. Having a high refractive index allows for sharp bends (of a few microns) without a significant increase in propagation loss.[17] As the bending radius of a flexible device is usually larger than a few millimeters, the loss introduced by the deformation itself is negligible compared to the scattering loss caused by surface roughness. This hybrid system also inherits the low absorption loss of single-crystal silicon. We have demonstrated stamp printing of single-crystal silicon nanomembrane-based multimode waveguides

* Address correspondence to xiaochuan.xu@utexas.edu, raychen@uts.cc.utexas.edu.

Received for review August 6, 2014 and accepted November 19, 2014.

Published online November 19, 2014
10.1021/nn504393j

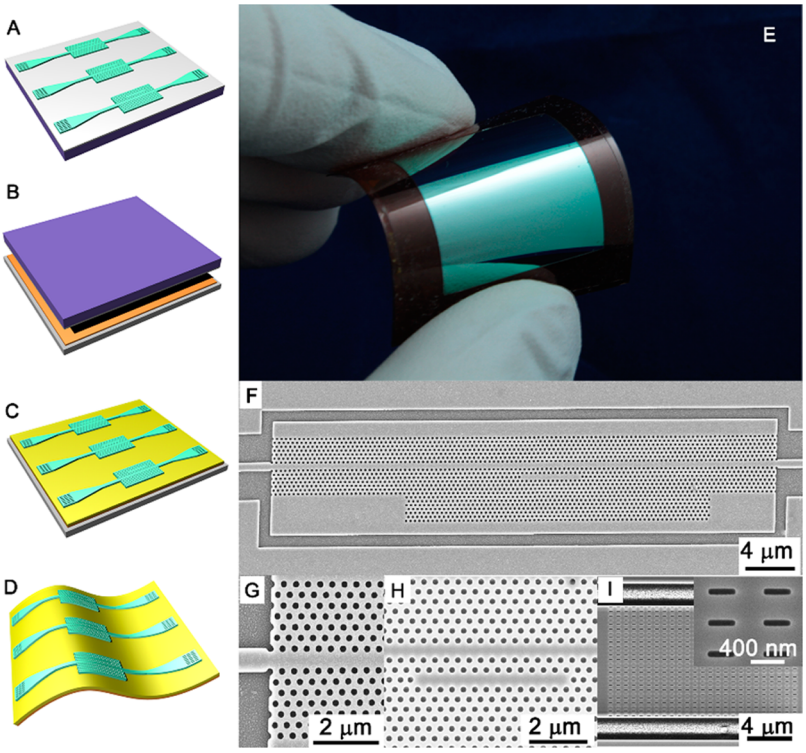

Figure 1. (A–D) Transfer process. (A) Pattern the photonic crystal microcavity on SOI. (B) Flip bond the SOI chip onto the polyimide film with SU-8 epoxy. (C) Remove the silicon handle and BOX layer with mechanical polishing, DRIE, and wet etching. (D) Peel off the polyimide film from the mechanical support. (E) Transferred 2 cm × 2 cm silicon nanomembrane on polyimide film. SEM image of (F) L13 photonic crystal microcavity, (G) input section of the photonic crystal waveguide, (H) magnified image of the transferred photonic crystal microcavity, and (I) SWG coupler.

onto polyimide films with a propagation loss of 1.1 dB/cm, which is comparable to the loss on a silicon-on-insulator (SOI) platform.[18] As usual, great opportunities are accompanied by great challenges. First, photonic devices are usually long in the longitudinal direction and short in the transverse direction, resulting in an aspect ratio exceeding a few thousand. This high aspect ratio cannot be accommodated by conventional stamp printing processes developed for flexible inorganic electronics. Moreover, the performance of photonic devices heavily relies on the integrity of its geometry with limited tolerance to geometrical defects. Although the stamp printing procedure does not have intrinsic limitations, the "peeling" and "printing" operations are more likely to generate geometrical defects due to engineering issues. This paper introduces a viable high yield transfer method, with which we demonstrate a flexible crystalline silicon photonic crystal microcavity which could be bent to a curvature of 5 mm radius, without any appreciable optical loss. The device's potential as a deformable sensor is also explored.

RESULTS AND DISCUSSION

Figure 1A–D briefly depicts the transfer sequence. A detailed description can be found in the Supporting Information. As shown in Figure 1A, the photonic devices are patterned on a 2 cm × 2 cm silicon-on-insulator (Soitec SOI) chip with a 250 nm single-crystal silicon layer, 3 μm buried oxide layer (BOX), and a 675 μm silicon handle using electron beam lithography and reactive ion etching (HBr/Cl_2). The patterned chip is flipped over and bonded onto a 125 μm thick polyimide substrate (Dupont Kapton HN) through adhesive bonding with SU-8 (Microchem) (Figure 1B). The native oxide on the SOI chip is removed by 1:6 buffered oxide etchant prior to bonding because the adhesion between SU-8 and SiO_2 is weak. Prior to bonding, the polyimide film is mounted on a rigid substrate. SU-8 is spin-coated on both the polyimide film and the SOI chip, both of which are baked at 65 °C for an extended period of time to improve surface quality as SU-8 has impressive self-planarization capability when heated above its glass transition temperature.[19,20] The SU-8 layer on the polyimide film is partially exposed to generate Lewis acid, which initiates cross-linking when the unexposed SU-8 on SOI is brought in contact. The pressure is applied by a homemade bonder, which is shown in Figure S3. After bonding, the silicon handle is removed by mechanical polishing followed by deep reactive ion etching (DRIE), as shown in Figure 1C. The DRIE process is tailored to reduce the processing temperature. The etch rate is about 2.7 μm/cycle with a selectivity of 80:1 to silicon dioxide (SiO_2), making the 3 μm thick BOX an excellent etch stop layer, which is then removed by concentrated 49% hydrofluoric acid. Finally, the

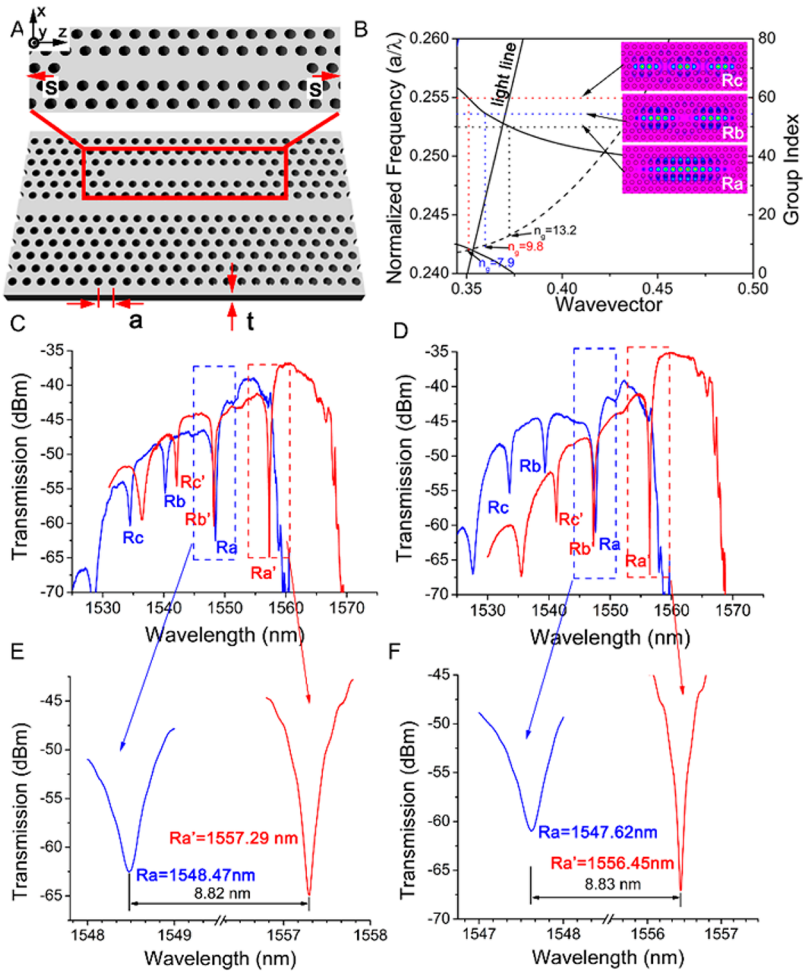

Figure 2. (A) Schematic of the L13 cavity. (B) Band diagram of the PCW (solid black curve). The L13 cavity resonance frequencies are indicated by dotted lines. Inset: $|H_y|^2$ of the three resonant modes. (C) Transmission spectra of the L13 PC microcavity device on SOI with deionized (DI) water as the top cladding (blue) and with glycerol as the top cladding (red). (D) Transmission spectra of the L13 PC microcavity device on polyimide film with DI water as the top cladding (blue) and with glycerol as the top cladding (red). (E) Zoomed-in image showing resonance R_a on SOI device with different top claddings. (F) Zoomed-in image showing resonance R_a on transferred device with different top claddings. Resonance wavelengths are also indicated in the figures.

polyimide film containing the silicon nanomembrane devices is peeled up from the rigid carrier (Figure 1D). Figure 1E shows the transferred 2 cm × 2 cm silicon nanomembrane. Figure S4 demonstrates that the film could be bent to a small curvature. The advantages of adhesive bonding include relatively low bonding temperatures, insensitivity to the bonding surface topology, and the ability to join virtually any two materials together. During the transfer procedure, SU-8 completely fills the holes and trenches in and around the photonic devices, providing mechanical support and protecting the delicate devices from mechanical failure. After transfer, oxygen plasma may be used to remove the SU-8 inside the holes for applications that require exposing the optical field to the outside world. Figure 1F–I shows the scanning electron microscope (SEM) images of the transferred L13 photonic crystal microcavity (Figure 1F–H) and the subwavelength grating (SWG) couplers (Figure 1I. Movie S1 in the Supporting Information shows that the film can bend, twist, and consistently return to its original form. It could also be cut as easily as a piece of paper.

Figure 2A illustrates the structure of the L13 photonic crystal microcavity comprising a linear photonic crystal microcavity side-coupled with a W1 photonic crystal waveguide (PCW). The cavity, which is formed by removing 13 holes along the Γ–K direction, is located two rows away from the W1 waveguide. The two holes at the two ends of the cavity are moved outward by a distance $s = 0.15a$ to reduce radiation loss and increase the quality factor (Q).[21] This optimized hole displacement is selected by experimentally comparing the Q of cavities with different hole shift.[21] The W1 PCW is formed by removing one row of holes along the Γ–K direction. The lattice constant a equals 393 nm in this work. The hole radius r is 108 nm, giving a r/a of 0.275. The thickness of the silicon slab t is 250 nm. An eight-period photonic crystal adiabatic taper is designed to improve the coupling efficiency between the strip waveguide and the PCW.[22] The

dispersion relation of the W1 PCW (solid curve) is simulated by three-dimensional plane wave expansion, as shown in Figure 2B. The resonance frequencies are also indicated by the dotted lines. The $|H_y|^2$ distribution of the resonant modes are shown in the inset of Figure 2B. Among the three resonances, resonances R_b and R_c are above the SiO_2 light line ($n \sim 1.45$ at 1550 nm), resulting in higher radiation loss and lower Q. Resonance R_a is of the most interest not only because of its high Q, but also because of its higher group index ($n_g \sim 13.2$), which provides greater interaction between the slowly traveling photons and analytes compared to a strip waveguide. For device characterization, SWGs are designed and integrated to couple light in and out of the transferred devices.[23] The transmission spectrum is obtained by analyzing the light coupled out from SWG with an optical spectral analyzer (OSA). The transmission spectra of the L13 cavity with water ($n \sim 1.33$ at 1550 nm) as its top cladding before and after being transferred to a new substrate are shown by the blue curves in Figure 2C,D. The presence of water, which is highly absorptive in the near-infrared wavelength range (absorbance: $\alpha \sim 800\ m^{-1}$ at 1550 nm), increases the absorption loss and lowers the Q to 9×10^3. After transfer, resonance R_a (1548.47 nm) blue shifts to 1547.62 nm, while the quality factor remains unchanged. The blue shift of resonances is due to the expansion of the holes induced by the transfer process. To determine the bulk sensitivity of the device, glycerol ($n \sim 1.46$ at 1550 nm) is dropped on top of the microcavity, and the transmission spectra from the devices on SOI and on polyimide are measured again, as indicated by the red curves in Figure 2C,D, respectively. The Q factor increases to 2.2×10^4 because glycerol is transparent in the wavelength range of interest. The resonance shift induced by the refractive index change of the top cladding is 8.82 nm, corresponding to a sensitivity of 68 nm/RIU (refractive index unit), which is comparable to the devices demonstrated on rigid SOI platforms.[24−26]

The bending characteristics of the flexible photonic crystal microcavity are investigated with the measurement setup shown in Figure 3. The two ends of the sample are constrained on the jaws of a caliper but allowed to rotate freely. The specimen is buckled upward or downward by sliding the movable jaw inward. The system allows the distance between the two jaws to be controlled with an accuracy better than 0.1 mm. Light is also coupled *via* single mode fibers into and out of the device through SWGs. The SWGs have been designed to have repeatable performance on curvatures with different bending radii. A detailed description of the SWGs is provided in the Supporting Information. The bending shape of the specimen can be approximated by a sinusoidal function (eq S3). The bending radius at the peak of the curvature is estimated by the second derivative of the sinusoidal curve,

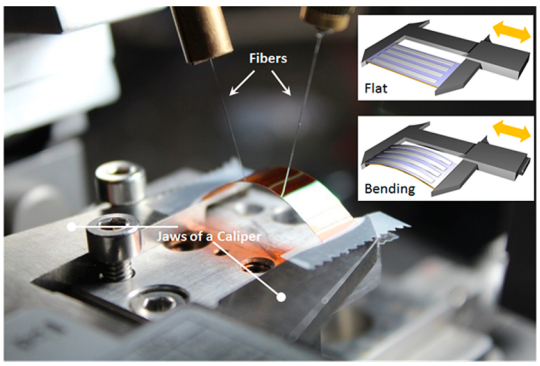

Figure 3. Configuration of the bending experiment. Inset: Sliding the movable jaws will buckle the specimen upward or downward.

as shown in eq S5.[27] We investigated four different types of axial bending: longitudinal face-out bending (LFO), longitudinal face-in bending (LFI), transverse face-out bending (TFO), and transverse face-in bending (TFI). For longitudinal bending, the bending direction is parallel to the light propagation direction (z axis), while it is perpendicular for transverse bending (x axis). In face-out bending (bending radius $R > 0$), the silicon nanomembrane experiences tensile stress in the bending direction, and in face-in bending ($R < 0$), it experiences compressive stress in the bending direction. The strain γ_{bend} of the silicon nanomembrane in the bending direction equals the distance from the neutral surface, d_n, divided by the bending radius R. The absolute value of R is between infinity (flat) and 5 mm. The corresponding absolute value of the strain $|\gamma_{bend}|$ in the bending direction is between 0 and 1.2%, as indicated in Figure S9. The experimentally observed shifts of resonance 1 in LFO, LFI, TFO, and TFI bending are shown by the red dots in Figure 4A−D, respectively. The resonance shifts to longer wavelength when the specimen is under tensile strain ($\gamma_{bend} > 0$) and to shorter wavelength when it is under compressive strain ($\gamma_{bend} < 0$). The strain sensitivity is summarized in Table 1. The resonant shift exhibits a linear correlation with strain. The sensitivities for LFO, LFI, TFO, and TFI are 0.673, 0.656, 0.588, and 0.591 pm/$\mu\varepsilon$, respectively, as calculated by linear regression. The device is observed to be slightly more sensitive to longitudinal bending than transverse bending.

The effects of bending are 2-fold: distort the geometry and transform the isotropic refractive index tensor into anisotropic. Geometrical distortion includes turning the circular holes into elliptical holes, changing the lattice structure, and altering the cavity properties. As the hexagonal lattice is distorted into a pseudohexagonal lattice, the hexagonal symmetry in the reciprocal lattice is broken and the irreducible Brillouin zone splits into three, shifting the photonic band gap structure and the guided mode, as shown qualitatively in the insets in Figure 4A−D.[28] Because of the asymmetry of the device, as implied in Figure 1F, the deformation

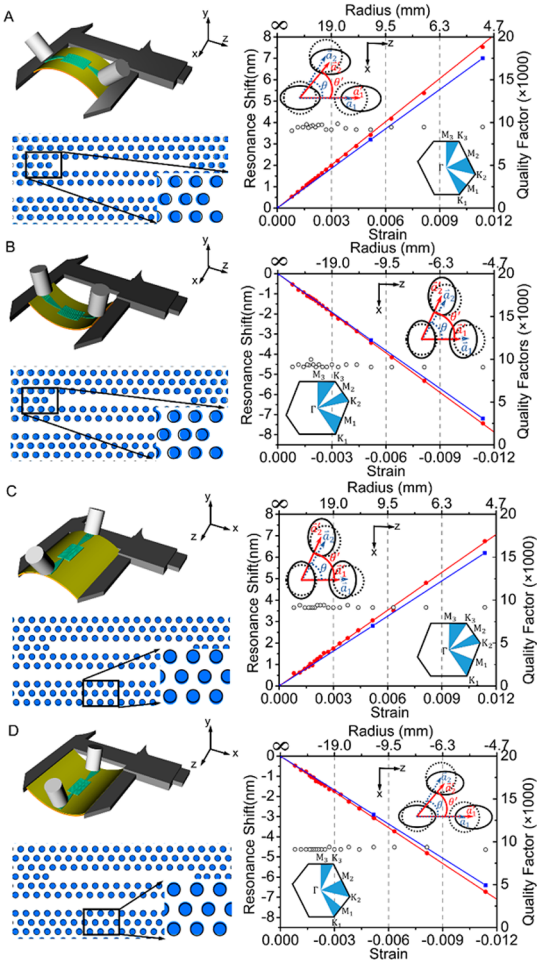

Figure 4. Bending characteristics of the transferred L13 PC microcavity under (A) LFO bending, (B) LFI bending, (C) TFO bending, and (D) TFI bending. The top left insets are the schematics depicting the bending configurations. The bottom left insets show the deformed geometries generated by FEM simulations. The right figures show the experimental (red) and simulation (blue) correlation between resonance R_a wavelength shift and strain. The insets in the right figures show the deformation of the holes and the corresponding distortion of the reciprocal lattice. The small black circles are the measured quality factors of the cavity at different bending radii.

TABLE 1. Strain Sensitivity (pm/$\mu\varepsilon$)

	LFO	LFI	TFO	TFI
experiment	0.673	0.656	0.588	0.591
simulation	0.616	0.633	0.545	0.563

is not symmetric either. Therefore, to give a precise account of the deformation, the whole device is simulated with finite element method (FEM) by prescribing corresponding displacements on the boundary. Since the dimension of the photonic crystal microcavity (10 μm × 40 μm) is much smaller than the minimum bending radius (5 mm), the strain could be closely approximated by in-plane uniaxial strain. The simulated deformed geometries are shown in the bottom left insets in Figure 4A–D, which show the deformation

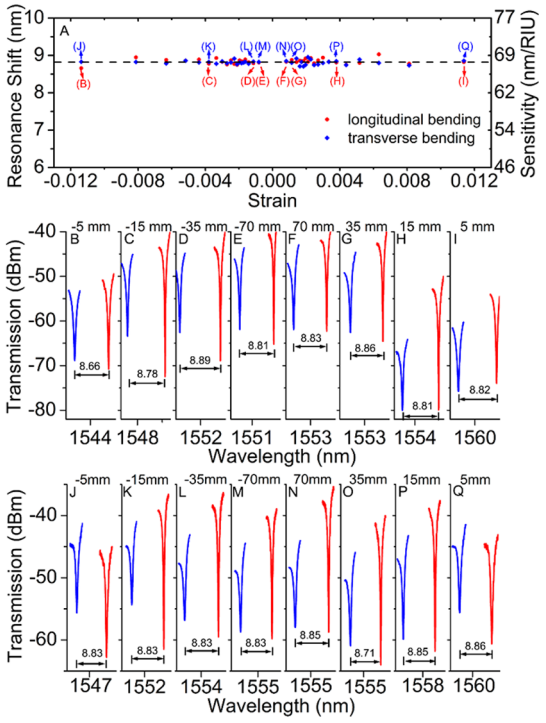

Figure 5. (A) Resonance shift caused by analytes with different refractive indices. A drop of analyte can be clearly seen adhering the surface even under bent conditions. (B-Q) Transmission spectra of resonance R_a in different bending cases: (B–E) LFO; (F–I) LFI; (J–M) TFO; (N–Q) TFI. For each bending case, four different bending radii are selected due to the limited space, including 5, 15, 35, and 70 mm. Blue curve: water top cladding. Red curve: glycerol top cladding.

and relocation of the holes. The L13 cavity is also altered by strain, leading to the change of its resonance property. As an example, the cavity is elongated under LFO bending, while its width shrinks due to Poisson's effect. In addition to the geometry distortion, the photoelastic effect also causes significant resonance shift. The relation between the components of the refractive index tensor and the stress can be calculated by eqs S9–S21. Due to the complexity of the structure, the exact calculation of stress as a function of position is prohibitive; thus, an averaged value is therefore adopted to estimate the refractive index tensor. The results are shown in Figure S9. Take LFO bending again as an example, n_{zz} increases while n_{xx} and n_{yy} decrease with increasing tensile strain. The deformed geometry and the refractive index tensors are used as input for finite-difference time-domain (FDTD) simulations. As the slab photonic crystal does not support pure transverse electric modes, all components of the refractive index tensor need to be considered in the FDTD simulations. The simulated resonance shift is shown by the blue lines in Figure 4A–D, which matches the experimental results with a discrepancy around 10%, possibly caused by errors induced due to approximations and utilizing the averaged stress values in the simulations. Another interesting phenomenon that has been observed is the Q of resonance R_a remains around

9×10^3 under different bending conditions due to the high index contrast between silicon and its cladding materials, as indicated by the black circles in Figure 4A–D.

As aforementioned, ultrathin monocrystalline devices are expected to not only exhibit excellent flexibility but also show comparable performance to their rigid counterparts. For a flexible and conformal photonic sensor, it would be even more valuable if its sensitivity is independent of the bending radius. To determine the effect of bending on sensitivity, measurements are performed with water and glycerol, just like the previous discussion. The results are summarized in Figure 5. A number of different bending radii have been investigated, and the results are summarized in Figure 5A. The device exhibits an average sensitivity of 68 nm/RIU under different bending conditions, which is identical to the sensitivity when the specimen lies flat. Four different bending radii (5, 15, 35, and 70 mm) are plotted in Figure 5B–Q for each bending configuration. The bending could delocalize the resonant mode field into the cladding and subsequently affect the sensitivity. In the face-out bending, for instance, the resonant mode field tends to delocalize into the top cladding. The overlap factor increases as the bending radius reduces, and thus the sensitivity could increase. Due to the relatively large bending radii and small strain, this phenomenon is negligible. The results also imply that the flexible photonic crystal microcavity can be reliably used on a curved surface.

CONCLUSION

We have demonstrated a flexible monocrystalline photonic crystal microcavity sensor using a bonding and silicon handle removal-based transfer technique. The demonstrated photonic crystal microcavity shows a quality factor up to 2.2×10^4. The high-performance sensor device could bend to a curvature of 5 mm radius without deteriorating the quality factor. The resonant wavelength shift is linearly correlated to the uniaxial strain. As a refractive index sensor, the flexible cavity demonstrates a deformation-independent sensitivity, which is crucial for real applications. This effort proves the feasibility of achieving intricate high-quality photonic devices on plastic substrates.

METHODS

Device Fabrication. The device is fabricated on commercially available silicon-on-insulator with 250 nm single-crystal silicon device layer, 3 μm buried oxide layer, and 675 μm silicon handle. The wafer is cleaved into 2 cm $\times$ 2 cm chips, and the chips are cleaned through a piranha bath. Hexamethyldisilazane is spin-coated at 4000 rpm for 35 s to enhance the adhesion between the electron beam resist and silicon. Electron beam resist ZEP520a is spin-coated at 6000 rpm for 35 s, giving a resist of 350 nm thickness. The pattern is transferred onto the resist by JBL 6000 and then to the silicon layer through reactive ion etching (HBr/Cl_2). The resist is stripped off by PG remover and a piranha bath.

Measurements. The bending tests are carried out by mounting the samples between the jaws of a Vernier caliper,[29] as illustrated in Figure 3 and its insets. The specimen is bent to a sinusoidal shape under a uniaxial compressive displacement applied by the movable jaw. Both ends of the specimen are linked to the jaws *via* Scotch tape but allowed to rotate almost freely in the vertical direction. This configuration can be approximated by the mechanical model of simply supported beams.[30] When the film is bent upward, it is defined as face-out bending and the silicon nanomembrane is subjected to a tensile stress. In contrast, as the film is bent downward, it is defined as face-in bending and the silicon nanomembrane is subjected to a compressive stress.[31] The study is performed on the specimen with an initial length of L. After applying a compressive displacement ΔL by the movable jaw, the specimen buckles and bends to an end-to-end length of $L - \Delta L$. ΔL can be measured by a caliper with an accuracy of 0.01 mm.

Light is coupled into devices through SWGs. A detailed discussion on SWGs is available in the Supporting Information. To characterize the devices, light from a broad-band source is polarized by a free space polarizer and delivered by a polarization maintaining fiber. The light from the output grating is harvested by a conventional single-mode fiber (SMF28) and analyzed by an OSA. Both the input and output fibers are held by copper tubes, which are mounted on 10° wedges sitting on *xyz* stages.

Conflict of Interest: The authors declare no competing financial interest.

Acknowledgment. The author would like to acknowledge Prof. J. Rogers at the University of Illinois at Urbana—Champaign for productive discussion. This research was funded by the Air Force Office of Scientific Research (AFOSR) Multidisciplinary University Research Initiative (MURI) under contract No. FA9550-08-1-0394 and Small Business Technology Transfer (STTR) under contract No. FA9550-11-C-0014 (program manager: Dr. G. Pomrenke), and by the National Institutes of Health (NIH) under contract No. HHSN2612012-00043C.

Supporting Information Available: Details of the fabrication process, grating coupler design and testing, mechanic analysis, and a video showing the flexible cavity. This material is available free of charge *via* the Internet at http://pubs.acs.org.

REFERENCES AND NOTES

1. Rogers, J. A.; Lagally, M. G.; Nuzzo, R. G. Synthesis, Assembly and Applications of Semiconductor Nanomembranes. *Nature* **2011**, *477*, 45–53.
2. Cavallo, F.; Lagally, M. G. Semiconductors Turn Soft: Inorganic Nanomembranes. *Soft Matter* **2010**, *6*, 439–455.
3. Huang, X.; Yeo, W. H.; Liu, Y. H.; Rogers, J. A. Epidermal Differential Impedance Sensor for Conformal Skin Hydration Monitoring. *Biointerphases* **2012**, *7*, 1–9.
4. Hwang, S. W.; Tao, H.; Kim, D. H.; Cheng, H. Y.; Song, J. K.; Rill, E.; Brenckle, M. A.; Panilaitis, B.; Won, S. M.; Kim, Y. S.; *et al.* A Physically Transient Form of Silicon Electronics. *Science* **2012**, *337*, 1640–1644.
5. Kim, D. H.; Ahn, J. H.; Choi, W. M.; Kim, H. S.; Kim, T. H.; Song, J. Z.; Huang, Y. G. Y.; Liu, Z. J.; Lu, C.; Rogers, J. A. Stretchable and Foldable Silicon Integrated Circuits. *Science* **2008**, *320*, 507–511.
6. Meitl, M. A.; Zhu, Z. T.; Kumar, V.; Lee, K. J.; Feng, X.; Huang, Y. Y.; Adesida, I.; Nuzzo, R. G.; Rogers, J. A. Transfer Printing by Kinetic Control of Adhesion to an Elastomeric Stamp. *Nat. Mater.* **2006**, *5*, 33–38.
7. Ying, M.; Bonifas, A. P.; Lu, N. S.; Su, Y. W.; Li, R.; Cheng, H. Y.; Ameen, A.; Huang, Y. G.; Rogers, J. A. Silicon Nanomembranes for Fingertip Electronics. *Nanotechnology* **2012**, *23*, 1–7.

8. Kim, R. H.; Tao, H.; Kim, T. I.; Zhang, Y. H.; Kim, S.; Panilaitis, B.; Yang, M. M.; Kim, D. H.; Jung, Y. H.; Kim, B. H.; *et al.* Materials and Designs for Wirelessly Powered Implantable Light-Emitting Systems. *Small* **2012**, *8*, 2812–2818.
9. Kim, D. H.; Ghaffari, R.; Lu, N. S.; Rogers, J. A. Flexible and Stretchable Electronics for Biointegrated Devices. *Annu. Rev. Biomed. Eng.* **2012**, *14*, 113–128.
10. Yoon, J.; Baca, A. J.; Park, S. I.; Elvikis, P.; Geddes, J. B.; Li, L. F.; Kim, R. H.; Xiao, J. L.; Wang, S. D.; Kim, T. H.; *et al.* Ultrathin Silicon Solar Microcells for Semitransparent, Mechanically Flexible and Microconcentrator Module Designs. *Nat. Mater.* **2008**, *7*, 907–915.
11. Park, S. I.; Xiong, Y. J.; Kim, R. H.; Elvikis, P.; Meitl, M.; Kim, D. H.; Wu, J.; Yoon, J.; Yu, C. J.; Liu, Z. J.; *et al.* Printed Assemblies of Inorganic Light-Emitting Diodes for Deformable and Semitransparent Displays. *Science* **2009**, *325*, 977–981.
12. Rogers, J. A.; Someya, T.; Huang, Y. G. Materials and Mechanics for Stretchable Electronics. *Science* **2010**, *327*, 1603–1607.
13. Kim, D. H.; Lu, N. S.; Ma, R.; Kim, Y. S.; Kim, R. H.; Wang, S. D.; Wu, J.; Won, S. M.; Tao, H.; Islam, A.; *et al.* Epidermal Electronics. *Science* **2011**, *333*, 838–843.
14. Song, Y. M.; Xie, Y. Z.; Malyarchuk, V.; Xiao, J. L.; Jung, I.; Choi, K. J.; Liu, Z. J.; Park, H.; Lu, C. F.; Kim, R. H.; *et al.* Digital Cameras with Designs Inspired by the Arthropod Eye. *Nature* **2013**, *497*, 95–99.
15. Ma, Z. Q.; Zhang, K.; Seo, J. H.; Zhou, H.; Sun, L.; Yuan, H. C.; Qin, G. X.; Pang, H. Q.; Zhou, W. D. Fast Flexible Electronics Based on Printable Thin Mono-crystalline Silicon. *ECS Trans.* **2011**, *34*, 137–142.
16. Zhou, H.; Seo, J. H.; Paskiewicz, D. M.; Zhu, Y.; Celler, G. K.; Voyles, P. M.; Zhou, W. D.; Lagally, M. G.; Ma, Z. Q. Fast Flexible Electronics with Strained Silicon Nanomembranes. *Sci. Rep.* **2013**, *3*, 1291.
17. Vlasov, Y. A.; McNab, S. J. Losses in Single-Mode Silicon-on-Insulator Strip Waveguides and Bends. *Opt. Express* **2004**, *12*, 1622–1631.
18. Xu, X. C.; Subbaraman, H.; Hosseini, A.; Lin, C. Y.; Kwong, D.; Chen, R. T. Stamp Printing of Silicon-Nanomembrane-Based Photonic Devices onto Flexible Substrates with a Suspended Configuration. *Opt. Lett.* **2012**, *37*, 1020–1022.
19. Stephan, K.; Gabriela, B.; Michael, L.; Daniel, H.; Anja, B. Processing of Thin SU-8 Films. *J. Micromech. Microeng.* **2008**, *18*, 125020.
20. Santeri, T.; Sami, F. Wafer-Level Bonding of MEMS Structures with SU-8 Epoxy Photoresist. *Phys. Scr., T* **2004**, *114*, 223–226.
21. Akahane, Y.; Asano, T.; Song, B. S.; Noda, S. High-*Q* Photonic Nanocavity in a Two-Dimensional Photonic Crystal. *Nature* **2003**, *425*, 944–947.
22. Johnson, S. G.; Bienstman, P.; Skorobogatiy, M. A.; Ibanescu, M.; Lidorikis, E.; Joannopoulos, J. D. Adiabatic Theorem and Continuous Coupled-Mode Theory for Efficient Taper Transitions in Photonic Crystals. *Phys. Rev. E* **2002**, *66*, 066608.
23. Xu, X. C.; Subbaraman, H.; Covey, J.; Kwong, D.; Hosseini, A.; Chen, R. T. Complementary Metal-Oxide-Semiconductor Compatible High Efficiency Subwavelength Grating Couplers for Silicon Integrated Photonics. *Appl. Phys. Lett.* **2012**, *101*, 031109.
24. Lai, W. C.; Chakravarty, S.; Zou, Y.; Chen, R. T. Silicon Nanomembrane Based Photonic Crystal Microcavities for High Sensitivity Bio-sensing. *Opt. Lett.* **2012**, *37*, 1208–1210.
25. Pal, S.; Guillermain, E.; Sriram, R.; Miller, B. L.; Fauchet, P. M. Silicon Photonic Crystal Nanocavity-Coupled Waveguides for Error-Corrected Optical Biosensing. *Biosens. Bioelectron.* **2011**, *26*, 4024–4031.
26. Yi, Z.; Chakravarty, S.; Kwong, D. N.; Wei-Cheng, L.; Xiaochuan, X.; Xiaohui, L.; Hosseini, A.; Chen, R. T. Cavity-Waveguide Coupling Engineered High Sensitivity Silicon Photonic Crystal Microcavity Biosensors with High Yield. *IEEE J. Sel. Top. Quantum Electron.* **2014**, *20*, 1–10.
27. Park, S. I.; Ahn, J. H.; Feng, X.; Wang, S. D.; Huang, Y. G.; Rogers, J. A. Theoretical and Experimental Studies of Bending of Inorganic Electronic Materials on Plastic Substrates. *Adv. Funct. Mater.* **2008**, *18*, 2673–2684.
28. Kim, S.; Gopalan, V. Strain-Tunable Photonic Band Gap Crystals. *Appl. Phys. Lett.* **2001**, *78*, 3015–3017.
29. Park, S.; Wang, G.; Cho, B.; Kim, Y.; Song, S.; Ji, Y.; Yoon, M. H.; Lee, T. Flexible Molecular-Scale Electronic Devices. *Nat. Nanotechnol.* **2012**, *7*, 438–442.
30. Timoshenko, S. P.; Gere, J. M. *Theory of Elastic Stability*, 2nd ed.; Dover Publications: Mineola, NY, 2009.
31. Ni, J. L.; Zhu, X. F.; Pei, Z. L.; Gong, J.; Sun, C.; Zhang, G. P. Comparative Investigation of Fracture Behaviour of Aluminium-Doped ZnO Films on a Flexible Substrate. *J. Phys. D: Appl. Phys.* **2009**, *42*, 175404.